

ARTICLE

Received 5 Mar 2015 | Accepted 11 Aug 2015 | Published 11 Sep 2015

DOI: 10.1038/ncomms9340

OPEN

Monolayered Bi_2WO_6 nanosheets mimicking heterojunction interface with open surfaces for photocatalysis

Yangen Zhou¹, Yongfan Zhang^{2,3}, Mousheng Lin¹, Jinlin Long¹, Zizhong Zhang¹, Huaxiang Lin¹, Jeffrey C.-S. Wu⁴ & Xuxu Wang¹

Two-dimensional-layered heterojunctions have attracted extensive interest recently due to their exciting behaviours in electronic/optoelectronic devices as well as solar energy conversion systems. However, layered heterojunction materials, especially those made by stacking different monolayers together by strong chemical bonds rather than by weak van der Waal interactions, are still challenging to fabricate. Here the monolayer Bi_2WO_6 with a sandwich substructure of $[\text{BiO}]^+ - [\text{WO}_4]^{2-} - [\text{BiO}]^+$ is reported. This material may be characterized as a layered heterojunction with different monolayer oxides held together by chemical bonds. Coordinatively unsaturated Bi atoms are present as active sites on the surface. On irradiation, holes are generated directly on the active surface layer and electrons in the middle layer, which leads to the outstanding performances of the monolayer material in solar energy conversion. Our work provides a general bottom-up route for designing and preparing novel monolayer materials with ultrafast charge separation and active surface.

¹State Key Laboratory of Photocatalysis on Energy and Environment, Fuzhou University, Fuzhou 350002, China. ²Department of Chemistry, Fuzhou University, Fuzhou 350108, China. ³Fujian Provincial Key Laboratory of Theoretical and Computational Chemistry, Xiamen 361005, China. ⁴Department of Chemical Engineering, National Taiwan University, Taipei 10617, Taiwan. Correspondence and requests for materials should be addressed to X.W. (email: xwang@fzu.edu.cn).

Semiconductor-based heterojunctions are able to facilitate fast charge separation, and thus have emerged as one of important strategies for creation of efficient solar energy conversion systems^{1–4}. It is well known that a heterojunction in nature is the interface that occurs between two dissimilar crystalline semiconductors. The heterojunction effect on charge separation are thought to come from the built-in electric field forming at the atomically thin interface¹. Compared with conventional powder heterojunction materials, the layered heterojunctions composed of different ultrathin two-dimensional (2D) materials have sparked widespread interests because of the well-defined heterostructures almost as thin as the interface of conventional heterojunctions. As great successes on monolayer materials have been achieved^{5–7}, the stacks of different monolayers held together by van der Waals forces have been realized^{8–15}. However, the layered heterojunctions composed of different monolayers stacked together by strong chemical bonds have been rarely studied. Since chemical bonding between

monolayers can greatly enhance charge separation and even induce new energy band structures, the layered heterojunctions are considerably appealing^{16,17}. Besides charge separation, exposure of active sites (mainly unsaturated atoms) is also key to affect the material performances in solar energy conversion^{18,19}. The monolayers from van der Waals layered materials (with layers stacked by van der Waals forces) such as MoS₂ have been found active sites only at the edge^{20–22}. Post-processing methods such as defect engineering have often been applied for creating more active sites on these 2D materials^{23–25}. Aurivillius phase oxides, as complex layered materials, consist of alternate stacking of [Bi₂O₂] layers and perovskite-type layers with oxygen atoms shared between layers. This means that such a monolayer material maybe regarded as the stacks of different monolayer oxides by chemical bonds, and may possess oxygen-depleted surfaces that expose a huge number of active sites.

It is well known that monolayer materials maybe achieved on a small scale by mechanical exfoliation or chemical vapour

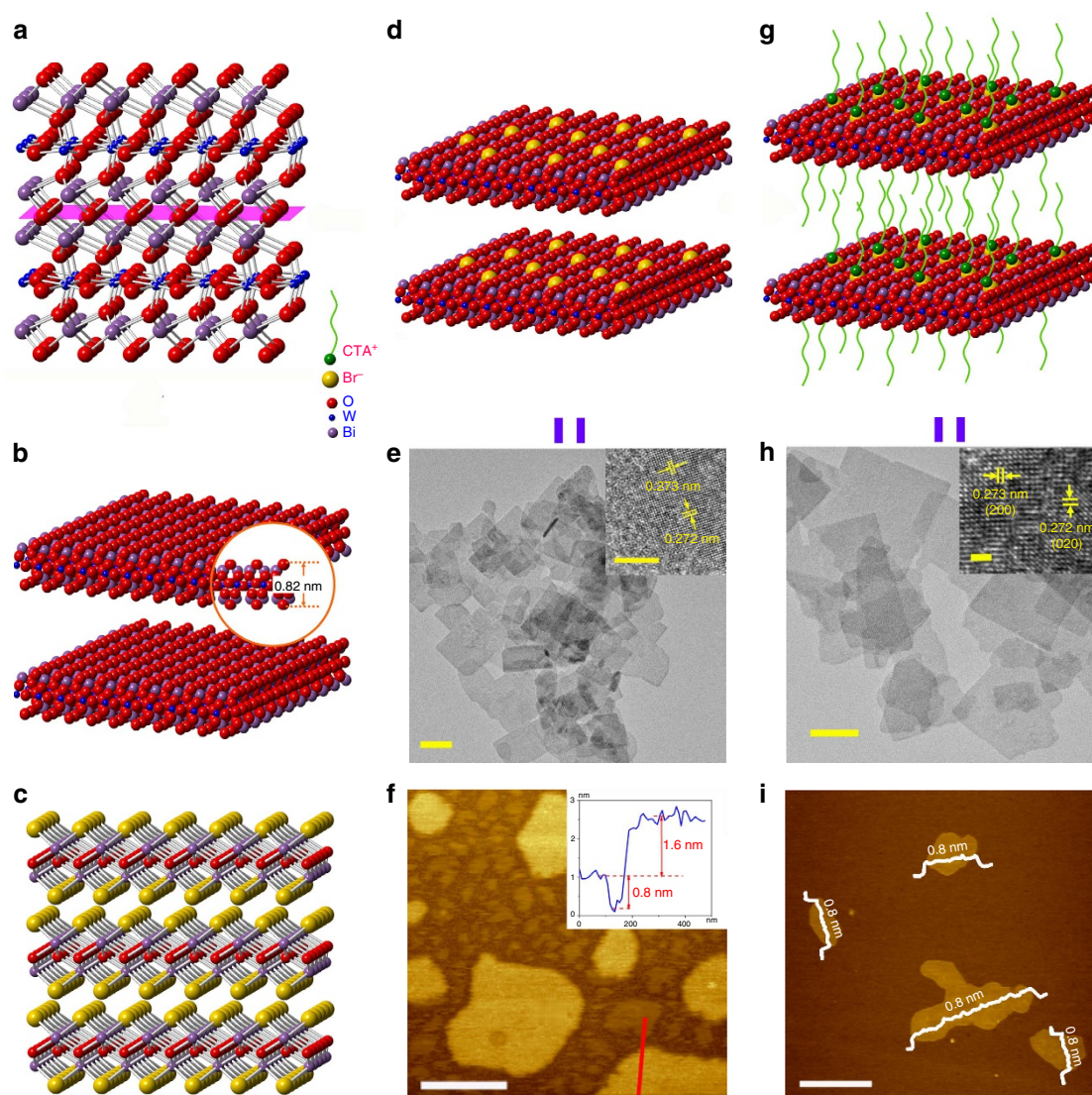


Figure 1 | Synthesis of monolayer Bi₂WO₆. (a) Crystal structure of Bi₂WO₆. (b) Structure of pristine monolayer Bi₂WO₆. (c) Crystal structure of BiOBr. (d) Formation mechanism of the monolayer Bi₂WO₆ with Br[−] ions assistance. (e) TEM image of the synthesized Bi₂WO₆ with Br[−] ions assistance; inset is the corresponding HRTEM image. (f) AFM image of the monolayer Bi₂WO₆ prepared by Br[−] ions assistance; inset is the corresponding height profile on the red line. (g) Formation mechanism of the monolayer Bi₂WO₆ with CTAB assistance. (h) TEM image and the corresponding HRTEM image of the Bi₂WO₆ prepared with CTAB assistance. (i) AFM image of the monolayer Bi₂WO₆ prepared by CTAB assistance. Scale bar, 500 nm (f,i), 50 nm (e,h), 5 nm (insets in e) and 1 nm (insets in h).

deposition^{26–28}. However, the practical and large-scale synthesis of freestanding monolayers in liquid phase is irreplaceable for many applications. Up to now, most monolayer materials are produced by liquid exfoliation of the van der Waals layered materials, such as graphene, boron nitride (BN) and transition metal dichalcogenides^{29–31}. However, it is difficult to exfoliate the layered materials with layers stacked by strong chemical bonds. The alternative method, a bottom-up approach, has been used to produce multilayer nanosheets, but rarely succeed in monolayer materials^{32,33}. The key to preparation of such monolayers by the bottom-up route is to keep monolayers from stacking together.

We develop a cetyltrimethylammonium bromide (CTAB)-assisted bottom-up route to fabricate such freestanding monolayer materials. The successfully synthesized monolayer Aurivillius oxide Bi_2WO_6 has a sandwich substructure of $[\text{BiO}]^+ - [\text{WO}_4]^{2-} - [\text{BiO}]^+$, mimicking heterojunction interface with space charge. The Br^- ions from CTAB strongly adsorb on the monolayers surfaces and thus make the monolayers negatively charged. In the self-assembly process, stacking of the monolayers is blocked by Coulomb repulsion forces and the hydrophobic chains of CTA^+ ions. The Br^- ions on surface induce a decrease in the bandgap energy of the monolayers. The surface Bi atoms are coordinatively unsaturated and thus the monolayers surfaces expose a huge number of active sites. On irradiation, holes are directly generated on the active surfaces and electrons in the middle layer, leading to ultrafast charge separation. Both the highly active surface and the ultrafast charge separation contribute to the superior photocatalytic performances of the monolayer material. In the presence of positive dyes, the visible light activity of the monolayers can be greatly enhanced due to photosensitization of the strongly adsorbed dye.

Results

Self-assembly of Bi_2WO_6 monolayers. As shown in Fig. 1a, Bi_2WO_6 is a layered material built up of $[\text{Bi}_2\text{O}_2]$ layers and corner-shared WO_6 octahedral layers. Monolayer Bi_2WO_6 has two possible configurations: $[\text{BiO}]^+ - [\text{WO}_4]^{2-} - [\text{BiO}]^+$ (sandwich substructure) and $[\text{Bi}_2\text{O}_2]^{2+} - [\text{WO}_4]^{2-}$ (non-sandwich substructure). Density functional theory (DFT) calculations show that the surface energy of the sandwich configuration is 0.86 J m^{-2} , notably smaller than that of the non-sandwich substructure (2.27 J m^{-2}). It can be deduced accordingly that the monolayer Bi_2WO_6 has the sandwich structure, as presented in Fig. 1b.

As mentioned above, the monolayer Bi_2WO_6 exposes coordinatively unsaturated Bi atoms on surface (Fig. 1b). This induces strong interaction between the monolayers and therefore makes the monolayers to stack easily into multilayers. So far no monolayer nanosheets have been achieved through bottom-up route^{33,34}. Obviously, weakening the interaction between the monolayers is a key to successfully obtain the monolayer material. It is well known that BiOBr is a typical layered material consisting of $(\text{Br}-\text{Bi}-\text{O}-\text{Bi}-\text{Br})$ slices stacked together by van der Waal interaction, in which the Br atoms terminate the dangling bonds of slices (Fig. 1c)³⁵. When Br^- ions were introduced in the bottom-up synthesis system for Bi_2WO_6 , they would bond to the monolayers surfaces to terminate the dangling bonds partly and make the surface negatively charged, which would suppress the stacking of the monolayers, as shown in Fig. 1d.

As expected, the monolayer Bi_2WO_6 was achieved when KBr as a Br^- source was added to the hydrothermal reaction system of $\text{Bi}(\text{NO}_3)_3 \cdot 5\text{H}_2\text{O}$ and $\text{Na}_2\text{WO}_4 \cdot 2\text{H}_2\text{O}$ (Br/Bi atomic ratio is 1:20). The X-ray diffraction patterns of the resulted sample are shown in Supplementary Fig. 1. All the diffraction peaks can

be indexed to an orthorhombic Bi_2WO_6 phase with lattice parameters $a = 5.457 \text{ \AA}$, $b = 5.436 \text{ \AA}$ and $c = 16.427 \text{ \AA}$ (JCPDS No. 73-2020). The transmission electron microscopy (TEM) image in Fig. 1e exhibits the synthesized Bi_2WO_6 with a sheet-shaped structure. Inset in Fig. 1e gives the corresponding high-resolution transmission electron microscopy (HRTEM) image. The marked interplanar spacings of (200) and (020) planes indicate that the Bi_2WO_6 nanosheets expose {001} facets. The atomic force microscopic (AFM) image and the corresponding height histograms of the nanosheets are presented in Fig. 1f and Supplementary Fig. 2, respectively. It can be seen that the thinnest nanosheets have a thickness of ca. 0.8 nm, which agrees well with that of monolayer Bi_2WO_6 sheet along [001] direction (corresponding to 1/2 of the unit cell size in c -axis direction). This shows that the Bi_2WO_6 monolayers can be achieved by a Br ions-assisted hydrothermal method. Unfortunately, some bilayer nanosheets are observed in the products.

CTAB is a long-chain cationic surfactant containing Br^- ions. When CTAB instead of KBr was used in the synthesis, the CTA^+ ions would adsorb on the surface with bonding of Br^- ions to the monolayers surfaces. Thus, the extra surface repulsion from the hydrophobic chains of CTA^+ further prevents stacking of the monolayers, as showed in Fig. 1g. In this case, the high-quality monolayer Bi_2WO_6 was successfully prepared. The X-ray diffraction result reveals that the obtained sample is pure phase Bi_2WO_6 (Supplementary Fig. 1). The sample shows weaker X-ray diffraction peaks than that prepared with only Br^- ions, indicating the smaller size of the sample. The TEM image (Fig. 1h) displays sheet-shaped structures of the sample. It can be seen from the HRTEM image (inset of Fig. 1h) that marked interplanar spacings of (200) and (020) planes appear on the sample, indicating the {001} exposed facets of the nanosheets. The AFM image in Fig. 1i shows that the thickness of nanosheets is very close to that of monolayer Bi_2WO_6 slab (the height histograms in Supplementary Fig. 3). These results illustrate that the well-defined Bi_2WO_6 monolayers were successfully prepared by the one-pot CTAB-assisted hydrothermal process.

In addition, a control synthesis with neither KBr nor CTAB assistance was also performed for comparison. Only the Bi_2WO_6 nanocrystals were obtained in this case. Both the TEM image (Supplementary Fig. 4) and the HRTEM image (Supplementary Fig. 5) show that the sample is 20 nm diameter near-spherical aggregation consisting of 8 nm diameter nanocrystals. The X-ray diffraction pattern of nanocrystals is the same as that of the monolayers obtained by CTAB assistance (Supplementary Fig. 6), indicating the same crystal phase. Above results show that the Br^- and CTA^+ are responsible for the formation of monolayer Bi_2WO_6 , which were further discussed in Supplementary Figs 7–9.

Chemical compositions of Bi_2WO_6 monolayers. X-ray photoelectron spectroscopic (XPS) characterizations were conducted to reveal the chemical compositions of the monolayer Bi_2WO_6 (ref. 36). The Br 3d, Bi 4f, W 4f and O 1s XPS spectra of the Bi_2WO_6 monolayers and nanocrystals are shown in the Fig. 2. For the monolayers, a strong Br 3d peak is observed at the binding energy of 68.5 eV, which suggests that the Br^- ions from CTAB are bonded to the surface Bi atoms of the monolayer³⁷. Compared with the nanocrystals, the monolayers present two asymmetric Bi 4f peaks (Fig. 2b), indicating the different chemical states of Bi for the two samples. Both the asymmetric Bi 4f peaks can be deconvoluted into two peaks. The shoulder peaks (165.0 eV for Bi 4f_{5/2}, and 159.9 eV for and Bi 4f_{7/2}) occur at higher binding energies, indicating higher electropositive Bi appearing in the monolayers. This can be indicative of some Bi atoms bonded with

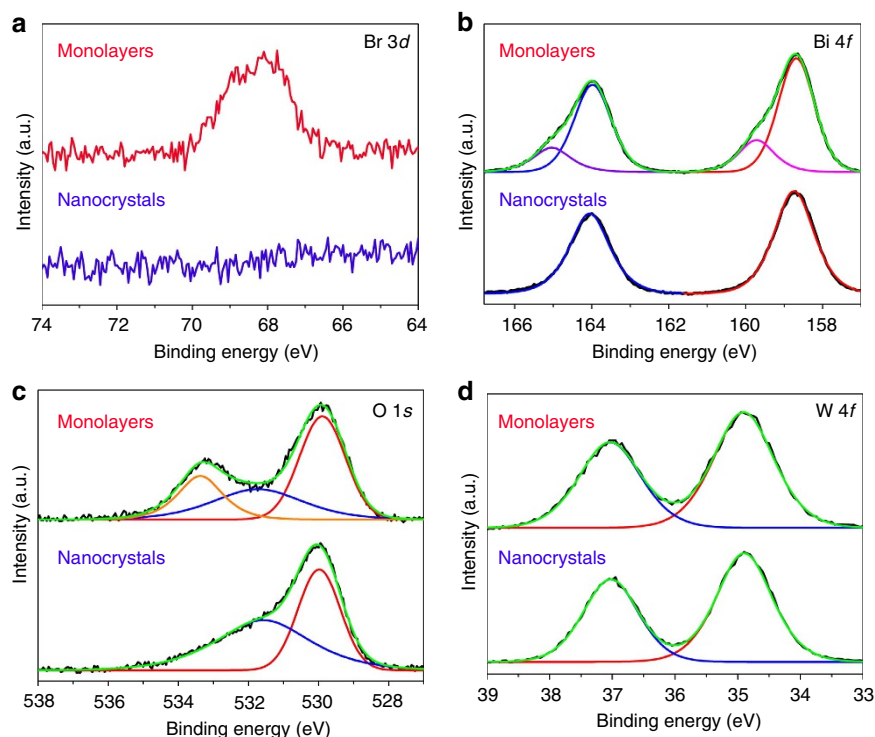


Figure 2 | XPS of Bi_2WO_6 samples. (a) Br 3d, (b) Bi 4f, (c) O 1s and (d) W 4f.

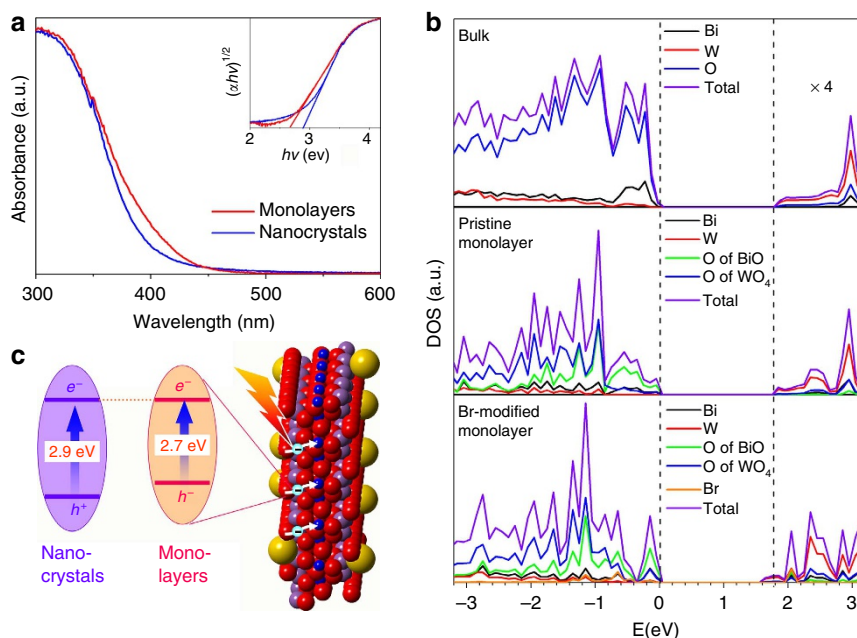


Figure 3 | Bandgap states of Bi_2WO_6 samples. (a) Diffuse reflectance ultraviolet-visible spectra of Bi_2WO_6 samples. (b) Calculated density of states (DOSs) of Bi_2WO_6 bulk, pristine monolayer and Br-modified monolayer. The Fermi level is taken as the energy zero. (c) Band energy diagrams of Bi_2WO_6 nanocrystals and monolayers. W, O, Bi and Br atoms are represented as blue, red, purple and yellow spheres, respectively.

the surface Br atoms³⁷. Figure 2c is O 1s spectra, two peaks at 529.9 eV and 531.7 eV are observed for both samples, which are assigned respectively to lattice oxygen and bridging hydroxyls³⁸. But the peak at 533.3 eV belonging to physisorbed water only appears for the monolayers³⁹. This is because the open metal sites on the monolayers surfaces have strong interaction with surrounding water. Figure 2d shows that the W 4f spectra are almost comparable for two samples, which can be explained by

$[\text{WO}_4]^{2-}$ locating at the middle layers of the monolayers and hardly affected by the surface Br atoms.

Quantitative XPS analysis shows that the ratios Br/Bi/W are 0.2/2.1/1.0 in the monolayer Bi_2WO_6 sample, of which the Bi/W ratio is almost identical to that of the nanocrystals. This result implies that the Br^- ions are non-stoichiometrically coordinated to $[\text{BiO}]^+$ layers together with the CTA^+ . An additional experiment shows that the CTA^+ ions on the monolayers

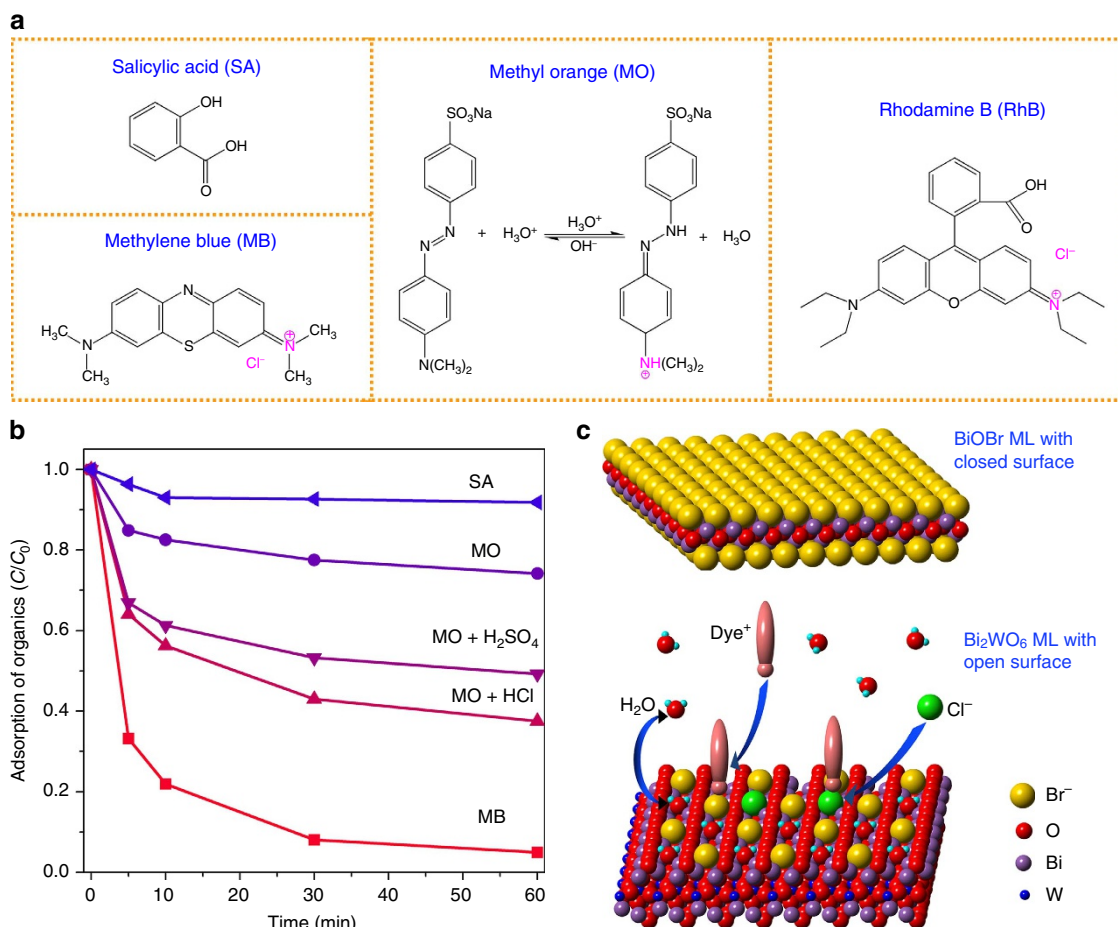


Figure 4 | Open surface of the Bi₂WO₆ monolayers. (a) Molecular structures of various organic contaminants. (b) Adsorption of various organic pollutants over the Bi₂WO₆ monolayers. (c) Schematic diagram showing the interactions between the open surface of monolayer Bi₂WO₆ and surrounding species.

surfaces can be removed by washing (Supplementary Fig. 10). H⁺ ions may substitute the CTA⁺ ions for keeping charge balance of the monolayer in the washing process. The residual amount of CTA⁺ ions on the surface are very low and no obvious influence was observed on the photocatalytic activity of the monolayers (Supplementary Figs 11–12).

Synthesis of other monolayer materials. To verify the universal applicability of this self-assembly route, preparation of monolayer Bi₂O₂CO₃ was studied also in the same conditions. The result shows that the monolayer Bi₂O₂CO₃ with a thickness of 0.55 nm was successfully obtained in the presence of CTAB, as showed in the Supplementary Figs 13–15. Besides Bi₂WO₆ and Bi₂O₂CO₃, the Aurivillius phase layered oxides (general formula Bi₂A_{n-1}B_nO_{3n+3}; A = Ca, Sr, Ba, Pb, Bi, Na, K and B = Ti, Nb, Ta, Mo, W, Fe), an important class of functional materials including photocatalysts, superconductors, and ferroelectric materials^{40–42}, have the common feature of containing [Bi₂O₂] layers in crystal structure. Thus, a huge number of monolayer Aurivillius materials can be formed by the similar mechanism of self-assembly.

Band gap of the monolayer Bi₂WO₆. Figure 3a shows ultraviolet–visible diffuse reflectance spectrum of the Bi₂WO₆ samples. The bandgap energies of the samples were estimated from the plots of $(\alpha h\nu)^{1/2}$ versus the energy of absorbed light (inset of Fig. 3a)⁴³. The bandgap energy of the monolayers is ca. 2.7 eV, lower than that of the nanocrystals by 0.2 eV. To

understand the differences, band structures of the bulk (multilayers), pure monolayer (unmodified) and Br-modified monolayer of Bi₂WO₆ were investigated theoretically (Supplementary Fig. 16). The corresponding densities of states are presented in Fig. 3b. Although the bandgaps from DFT calculations are usually smaller than that from the experimental determination, the DFT calculations often provide important insights into the physicochemical properties of the materials^{43,44}. For the unmodified monolayers and the bulk, the top of valence band and the bottom of conduction band are mainly originated from hybrid Bi 6s–O 2p orbital and W 5d orbital, respectively (Fig. 3b). However for the Br-modified monolayers, the bottom of conduction band is still originated from W 5d orbital, but the top of valence band is composed of the hybridized orbital of Bi 6s, O 2p and Br 4p (Fig. 3b). Due to more negative potential of their top of valence, the Br-modified monolayers show a narrower bandgap than the unmodified monolayers and the nanocrystals.

The sandwich substructure of [BiO]⁺–[WO₄]²⁻–[BiO]⁺ of monolayer Bi₂WO₆ simulates the heterojunction interface with space charge that promotes separation of the photogenerated carriers in the interface, as shown in Fig. 3c. It should be noted that the bottom of conduction band is originated from W 5d orbital located in the middle layer, and the top of valence band is mainly composed of O 2p orbital from the surface [BiO]⁺ layers (Fig. 3b). On irradiation, holes and electrons can be generated, respectively, on the surface layer and in the middle layer and thus are separated directly. In brief, for the monolayer Bi₂WO₆, the

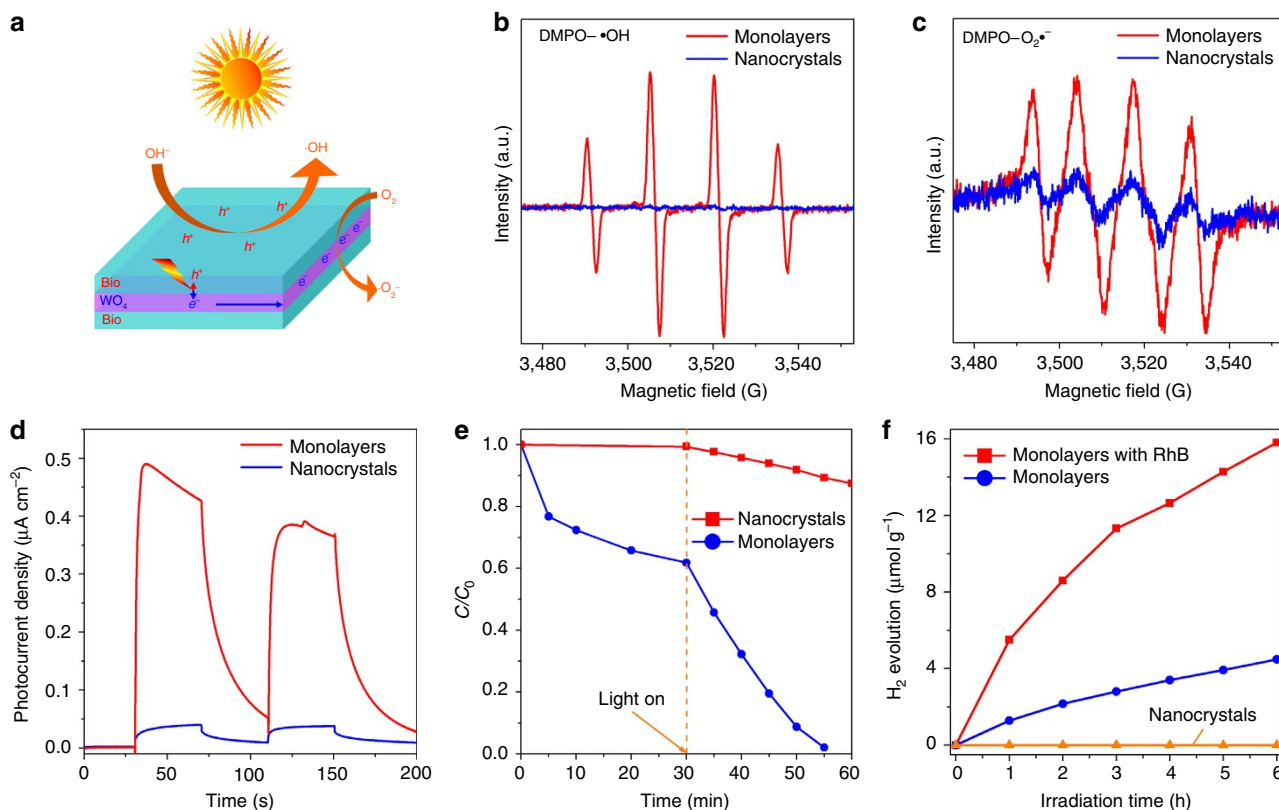


Figure 5 | Photocatalytic performances of Bi_2WO_6 samples. (a) Schematic illustration of photocatalytic mechanism over the monolayer Bi_2WO_6 . (b,c) Electron spin resonance signals of $\text{DMPO} \cdot \text{OH}$ adducts and $\text{DMPO} \cdot \text{O}_2^{\cdot -}$ adducts produced by Bi_2WO_6 samples under visible light irradiation ($\lambda \geq 420 \text{ nm}$). (d) Photocurrent of Bi_2WO_6 samples under visible light illumination. (e) Photodegradation of RhB over Bi_2WO_6 samples ($\lambda \geq 420 \text{ nm}$). (f) Visible-light-driven photocatalytic H_2 evolution over the nanocrystals, monolayers and RhB sensitized monolayers ($\lambda \geq 420 \text{ nm}$); 0.3 wt% of Pt was loaded.

sandwich substructure and the Br surface modification lead to decrease of the bandgap and enhancement of the photogenerated charges separation, which are very favourable for photocatalysis.

Open surface of the monolayer Bi_2WO_6 . Different from most reported monolayer materials with closed and inert surfaces²¹, the as-synthesized monolayer Bi_2WO_6 possesses oxygen-depleted and highly active surface. Moreover, the Br^- ions on surfaces cause the monolayers negatively charged, as proved by the zeta potential in Supplementary Table 1. Therefore, the monolayers can selectively adsorb positively charged species. Figure 4b shows the adsorption performances of various organic pollutants over the Bi_2WO_6 monolayers. Salicylic acid, as a neutral species, is hardly adsorbed by the monolayers. Methyl orange is positively charged in acid medium (Fig. 4a), and therefore its adsorption is enhanced by changing solution pH from 7 to 3 using H_2SO_4 or HCl . Similar to Br^- ions, Cl^- could also adsorb at the open metal sites on surface and make the monolayers more negatively charged, as shown in Fig. 4c. Hence, the methyl orange adsorption can be promoted more effectively by HCl than by H_2SO_4 . Methylene blue molecules containing both Cl^- ions and positive ammonium groups are adsorbed almost entirely. Owing to the open surfaces, the monolayers show much better ability for adsorption of Rhodamine B (RhB; 7.3 mg g^{-1}) than the nanocrystals (0.19 mg g^{-1}), though the specific surface area of the monolayers ($43 \text{ m}^2 \text{ g}^{-1}$) is less than twice that of the nanocrystals ($28 \text{ m}^2 \text{ g}^{-1}$). All above results confirm that the surface of monolayer Bi_2WO_6 is open and can strongly interact with surrounding species such as water, anions Cl^- or Br^- and positively charged organics (Fig. 4c).

Photocatalytic performance of the monolayer Bi_2WO_6 . Since the holes are photogenerated directly on the open surface $[\text{BiO}]^+$ layers (Fig. 5a), the monolayers surfaces are highly active for photocatalytic oxidation reactions, such as the oxidation of OH^- to $\cdot\text{OH}$. This feature was verified by the 5, 5-dimethyl-1-pyrroline-N-oxide (DMPO) spin-trapping electron paramagnetic resonance (EPR) technique (Fig. 5b). The $\cdot\text{OH}$ radicals signal is very weak for the nanocrystals under visible light illumination, which is consistent with the previously observation for Bi_2WO_6 samples⁴⁵. However, for the monolayer Bi_2WO_6 , the $\cdot\text{OH}$ radicals signal is much stronger, implying the superior activity of the monolayers for the photocatalytic oxidation reactions. On the other hand, the photoelectrons are formed in the middle layer where they transfer to the edge of monolayers for reduction reactions. Figure 5c shows that the reduction activity of the monolayers for O_2 to $\text{O}_2^{\cdot -}$ is enhanced likewise, compared with that of the nanocrystals, although the enhancement is lower for the reduction than for the oxidation. Figure 5d is comparison of photocurrents between the monolayers and nanocrystals. It can be seen that the photocurrent from the monolayers is about 10-fold higher than that from the nanocrystals. This indicates that the monolayers mimic the heterojunction interface to result in the ultrafast charge transfer and separation. As for the little decrease of photocurrent on the monolayers with irradiation time, this can be because the photogenerated electrons formed in the middle layer need to undergo a long-distance transfer towards the edge, electron accumulation and partial recombination with holes may occur simultaneously with irradiation time.

The photocatalytic performances of Bi_2WO_6 samples for photodegradation of RhB were evaluated under visible light

illumination ($\lambda \geq 420$ nm). As shown in Fig. 5e, the monolayers show much higher visible-light-driven photocatalytic activity than the nanocrystals. Ninety-eight percent of RhB are degraded using the monolayers as a photocatalyst within 25 min, while only 13% RhB are degraded using the nanocrystals within 30 min. Moreover, the monolayers can be efficiently recycled and reused without appreciable loss of activity (Supplementary Figs 17–18). Besides, the monolayers show also an excellent photocatalytic activity for H_2 production from water solution under visible light. Figure 5f shows the H_2 evolution over the nanocrystals, monolayers and RhB sensitized monolayers ($\lambda \geq 420$ nm) with 0.3 wt% Pt loading as a function of time. The H_2 evolution activity of Bi_2WO_6 has been reported to be very low ($1.6 \mu\text{mol h}^{-1} \text{g}^{-1}$) even under a 450 W high pressure mercury lamp⁴⁶. And the Bi_2WO_6 has been considered to have no activity for visible-light-driven H_2 production⁴⁷. As shown in Fig. 5f, the nanocrystals show indeed no H_2 evolution activity, but surprisingly the monolayers exhibit a good H_2 evolution activity under visible light. As adding RhB into the reaction system, ca. fourfold higher activity is observed due to the sensitization effect of RhB. Both the ultrafast charge separation and the highly active surface make the monolayers possess superior performances in solar energy conversion than other nanostructures composed of two or more layers (Supplementary Figs 19–21).

Discussion

In summary, the freestanding monolayer Bi_2WO_6 can be successfully synthesized via a CTAB-assisted self-assembly route. The as-synthesized monolayer Bi_2WO_6 has a sandwich substructure of $[BiO]^+ - [WO_4]^{2-} - [BiO]^+$. The Bi atoms in the surface $[BiO]^+$ layers are coordinatively unsaturated and thus the monolayers can adsorb Br^- ions to avoid stacking into multilayer. The monolayer Bi_2WO_6 shows oxygen-depleted surface, and has a narrower bandgap than the nanocrystals. The sandwich structure simulates the heterojunction interface with space charge to facilitate the ultrafast separation of photogenerated carriers. On irradiation, holes are generated directly on the highly active surfaces, resulting in the excellent activities for the photodegradation of RhB. More interestingly, the monolayering allows Bi_2WO_6 to have a visible-light-driven H_2 evolution activity, which can be efficiently enhanced by dye sensitization. This work provides a simple and efficient bottom-up route to prepare novel monolayer materials with ultrafast charge separation and highly active surface.

Methods

Materials synthesis. In the preparation of Bi_2WO_6 monolayers, the start materials 1 mmol $Na_2WO_4 \cdot 2H_2O$, and 2 mmol $Bi(NO_3)_3 \cdot 5H_2O$ and 0.05 g CTAB were added in 80 ml deionized water. After 30 min stirring, the mixed solution was poured into a 100 ml Teflon-lined autoclave. Then the autoclave was sealed into a stainless steel tank and treated at 120 °C for 24 h. Finally, the product was collected and washed several times with deionized water and dried at 60 °C in air for 10 h. In the preparation of monolayer Bi_2WO_6 accompanied with few layers, 0.1 mmol KBr instead of CTAB was added in the mixture, while keeping other parameters unchanged. The Bi_2WO_6 nanocrystals were prepared without CTAB and KBr assistances.

$Bi_2O_2CO_3$ monolayers were prepared by the same route. A total of 2 mmol $Bi(NO_3)_3$ and 0.05 g CTAB were added in 80 ml of 1 M HNO_3 solution. After the mixture became a clear solution, 10 mmol Na_2CO_3 was added and a white precipitate appeared immediately. This suspension was magnetically stirred for 30 min to complete the precipitation reaction. Then the suspension was poured into a 100 ml Teflon-lined autoclave and the autoclave was sealed into a stainless steel tank. The sample was treated at 60 °C for 24 h. Then the reactor was naturally cooled to room temperature. The obtained sample was collected and washed several times with deionized water and dried at 60 °C in air for 10 h.

Materials characterization. The X-ray diffraction patterns were recorded on a Bruker D8 Advance X-ray diffractometer with Ni filtered $Cu K\alpha$ radiation at 40 kV and 40 mA. Ultraviolet–visible diffuse reflectance (ultraviolet–visible diffuse reflectance spectrum) spectra were obtained with a self-supporting sample disk on a ultraviolet–visible spectrophotometer (Cary 500), where $BaSO_4$ was used as a

reflectance standard. TEM images were obtained using a JEOL model JEM 2010 EX instrument at an accelerating voltage of 200 kV. AFM images were recorded using Agilent 5,500 AFM (Agilent Technologies, USA). All the images were acquired using tapping mode under ambient conditions (ca. 40–50% relative humidity, 25 °C temperature). The used Si cantilevers/tips (Bruker) have a spring constant of 40 N m^{-1} and a resonance frequency of 300 kHz. During an AFM experiment, sample was dispersed in ethanol using an ultrasonic bath for 20 min and then the dispersion was diluted in ethanol. A drop of the above diluted dispersion was deposited on a new cleaved mica surface and dried in air. The instrument parameters (set point, amplitude, scan size, scan speed and feedback control) were adjusted for the best resolution of images. Electron spin resonance spectra were obtained over Bruker ESP 300 E electron paramagnetic resonance spectrometer.

Activity evaluation. The photodegradation of dyes were performed in a glass vessel under visible-light irradiation by a 300 W Xe lamp with a 420 nm cutoff filter. Twenty milligram of the photocatalyst was added into 80 ml RhB ($10 \mu\text{mol l}^{-1}$) solution. The dispersion was stirred in the dark for 30 min to reach the adsorption equilibrium. Then the visible light was turned on for the photodegradation tests. Three millilitres of the sample solution were taken at given time intervals and separated by centrifugation. The residual concentration of the organics in solution was analysed using a Varian Cary 50 Scan ultraviolet–visible spectrophotometer. The selective adsorption experiments were performed by the same method. The methyl orange (20 p.p.m.), methylene blue (10 p.p.m.) and salicylic acid ($500 \mu\text{mol l}^{-1}$) solutions were used. 50 mg of the catalyst was used to test the adsorption performances.

The photocatalytic H_2 production of samples under visible light irradiation was conducted in a Pyrex reactor connected with a gas-closed circulation system and a vacuum system. In a typical experiment, 20 mg catalyst was dispersed in 100 ml deionized water containing 0.4 g ethylenediamine tetraacetic acid (EDTA) as a sacrificial reagent. This system was evacuated for 30 min to remove air prior to irradiation. A 300-W Xe lamp with an optical cutoff filter ($\lambda \geq 420$ nm) was used as a light source. The produced hydrogen was quantified by gas chromatography (Shimadzu GC-8A, TCD, Ar carrier). For the RhB sensitization system, RhB ($10 \mu\text{mol l}^{-1}$) was contained in solution.

Calculation details. First-principles DFT calculations were carried out utilizing the Vienna *ab initio* simulation package^{48,49}. The Perdew–Wang-type (PW91) exchange–correlation functional was employed to study the energies and structures of different Bi_2WO_6 systems. Vanderbilt ultrasoft pseudo-potentials were used to describe the interactions between the ion cores and valence electrons for all atoms, and the kinetic cutoff energy was set to 400 eV. In the calculations, the convergence energy threshold for self-consistent iteration was set to 10^{-4} eV per atom, along with the residual atomic forces were $<0.03 \text{ eV \AA}^{-1}$. For the bulk Bi_2WO_6 , the optimized lattice constants are $a = 5.480 \text{ \AA}$, $b = 5.468 \text{ \AA}$ and $c = 16.760 \text{ \AA}$, which agrees well with the experimental values of $a = 5.457 \text{ \AA}$, $b = 5.436 \text{ \AA}$ and $c = 16.427 \text{ \AA}$. A (2×2) periodic slab model was adopted to simulate different Bi_2WO_6 nanosheets, which were constructed from the Bi_2WO_6 (001) surface. During the structural optimization, the positions of all atoms and the lengths of two translation vectors of the nanosheet were allowed to relax. The spacing between the adjacent slabs was set about 10 Å, and a $(3 \times 3 \times 1)$ Monkhorst–Pack k -point mesh was used for integration in the reciprocal space. To investigate the thermodynamic stability of different Bi_2WO_6 nanosheets, the surface free energy (γ) was calculated, which is defined as following,

$$\gamma = \frac{E^{\text{slab}} - NE_{Bi_2WO_6}^{\text{bulk}} - N_{Br}E_{Br}}{2A} \quad (1)$$

where E^{slab} is the total energy of the slab, $E_{Bi_2WO_6}^{\text{bulk}}$ is the energy of per Bi_2WO_6 unit in the bulk, N is the number of Bi_2WO_6 unit found in the slab, N_{Br} is the number of Br atom, E_{Br} is the ground state energy of Br atom, and A is the area of the slab surface.

References

- Wang, H. *et al.* Semiconductor heterojunction photocatalysts: design, construction, and photocatalytic performances. *Chem. Soc. Rev.* **43**, 5234–5244 (2014).
- Yuan, Y.-P., Ruan, L.-W., Barber, J., Joachim Loo, S. C. & Xue, C. Hetero-nanostructured suspended photocatalysts for solar-to-fuel conversion. *Energy Environ. Sci.* **7**, 3934–3951 (2014).
- Marschall, R. Semiconductor composites: strategies for enhancing charge carrier separation to improve photocatalytic activity. *Adv. Funct. Mater.* **24**, 2421–2440 (2014).
- Li, H., Zhou, Y., Tu, W., Ye, J. & Zou, Z. State-of-the-art progress in diverse heterostructured photocatalysts toward promoting photocatalytic performance. *Adv. Funct. Mater.* **25**, 998–1013 (2015).
- Xu, M., Liang, T., Shi, M. & Chen, H. Graphene-like two-dimensional materials. *Chem. Rev.* **113**, 3766–3798 (2013).
- Chhowalla, M. *et al.* The chemistry of two-dimensional layered transition metal dichalcogenide nanosheets. *Nat. Chem.* **5**, 263–275 (2013).

7. Butler, S. Z. *et al.* Progress, challenges, and opportunities in two-dimensional materials beyond graphene. *ACS Nano* **7**, 2898–2926 (2013).
8. Geim, A. K. & Grigorieva, I. V. Van der Waals heterostructures. *Nature* **499**, 419–425 (2013).
9. Wang, H. *et al.* Two-dimensional heterostructures: fabrication, characterization, and application. *Nanoscale* **6**, 12250–12272 (2014).
10. Duan, X. *et al.* Lateral epitaxial growth of two-dimensional layered semiconductor heterojunctions. *Nat. Nanotechnol.* **9**, 1024–1030 (2014).
11. Tan, C. *et al.* Liquid-phase epitaxial growth of two-dimensional semiconductor hetero-nanostructures. *Angew. Chem. Int. Ed.* **54**, 1841–1845 (2015).
12. Gong, Y. *et al.* Vertical and in-plane heterostructures from WS₂/MoS₂ monolayers. *Nat. Mater.* **13**, 1135–1142 (2014).
13. Hong, X. *et al.* Ultrafast charge transfer in atomically thin MoS₂/WS₂ heterostructures. *Nat. Nanotechnol.* **9**, 682–686 (2014).
14. Hou, Y. *et al.* Layered nanojunctions for hydrogen-evolution catalysis. *Angew. Chem. Int. Ed.* **52**, 3621–3625 (2013).
15. Lin, B. *et al.* Interstratified nanohybrid assembled by alternating cationic layered double hydroxide nanosheets and anionic layered titanate nanosheets with superior photocatalytic activity. *J. Hazard. Mater.* **280**, 156–163 (2014).
16. Zhang, H., Lv, X., Li, Y., Wang, Y. & Li, J. P25-graphene composite as a high performance photocatalyst. *ACS Nano* **4**, 380–386 (2010).
17. Huang, Q. *et al.* Enhanced photocatalytic activity of chemically bonded TiO₂/graphene composites based on the effective interfacial charge transfer through the C–Ti Bond. *ACS Catal.* **3**, 1477–1485 (2013).
18. Sun, Y., Gao, S., Lei, F. & Xie, Y. Atomically-thin two-dimensional sheets for understanding active sites in catalysis. *Chem. Soc. Rev.* **44**, 623–636 (2015).
19. Guan, M. *et al.* Vacancy associates promoting solar-driven photocatalytic activity of ultrathin bismuth oxychloride nanosheets. *J. Am. Chem. Soc.* **135**, 10411–10417 (2013).
20. Klein, A. *et al.* Schottky barriers on layered semiconductors: a comparison between van der Waals and non van der Waals faces. *Appl. Surf. Sci.* **70–71**, 470–474 (1993).
21. Jaramillo, T. F. *et al.* Identification of active edge sites for electrochemical H₂ evolution from MoS₂ nanocatalysts. *Science* **317**, 100–102 (2007).
22. Asadi, M. *et al.* Robust carbon dioxide reduction on molybdenum disulfide edges. *Nat. Commun.* **5**, 4470 (2014).
23. Kibsgaard, J., Chen, Z., Reinecke, B. N. & Jaramillo, T. F. Engineering the surface structure of MoS₂ to preferentially expose active edge sites for electrocatalysis. *Nat. Mater.* **11**, 963–969 (2012).
24. Xie, J. *et al.* Defect-rich MoS₂ ultrathin nanosheets with additional active edge sites for enhanced electrocatalytic hydrogen evolution. *Adv. Mater.* **25**, 5807–5813 (2013).
25. Xie, J. *et al.* Controllable disorder engineering in oxygen-incorporated MoS₂ ultrathin nanosheets for efficient hydrogen evolution. *J. Am. Chem. Soc.* **135**, 17881–17888 (2013).
26. Novoselov, K. S. *et al.* Two-dimensional atomic crystals. *Proc. Natl Acad. Sci. USA* **102**, 10451–10453 (2005).
27. Li, X. *et al.* Large-area synthesis of high-quality and uniform graphene films on copper foils. *Science* **324**, 1312–1314 (2009).
28. Lee, Y.-H. *et al.* Synthesis of large-area MoS₂ atomic layers with chemical vapor deposition. *Adv. Mater.* **24**, 2320–2325 (2012).
29. Nicolosi, V., Chhowalla, M., Kanatzidis, M. G., Strano, M. S. & Coleman, J. N. Liquid exfoliation of layered materials. *Science* **340**, 1226419 (2013).
30. Coleman, J. N. *et al.* Two-dimensional nanosheets produced by liquid exfoliation of layered materials. *Science* **331**, 568–571 (2011).
31. Osada, M. & Sasaki, T. Exfoliated oxide nanosheets: new solution to nanoelectronics. *J. Mater. Chem.* **19**, 2503–2511 (2009).
32. Sun, Z. *et al.* Generalized self-assembly of scalable two-dimensional transition metal oxide nanosheets. *Nat. Commun.* **5**, 3813 (2014).
33. Zhang, C. & Zhu, Y. Synthesis of square Bi₂WO₆ nanoplates as high-activity visible-light-driven photocatalysts. *Chem. Mater.* **17**, 3537–3545 (2005).
34. Tian, J. *et al.* A Bi₂WO₆-based hybrid photocatalyst with broad spectrum photocatalytic properties under UV, visible, and near-infrared irradiation. *Adv. Mater.* **25**, 5075–5080 (2013).
35. Li, J., Yu, Y. & Zhang, L. Bismuth oxyhalide nanomaterials: layered structures meet photocatalysis. *Nanoscale* **6**, 8473–8488 (2014).
36. Mann, A. K. P., Steinmiller, E. M. P. & Skrabalak, S. E. Elucidating the structure-dependent photocatalytic properties of Bi₂WO₆: a synthesis guided investigation. *Dalton Trans.* **41**, 7939–7945 (2012).
37. Feng, Y., Li, L., Li, J., Wang, J. & Liu, L. Synthesis of mesoporous BiOBr 3D microspheres and their photodecomposition for toluene. *J. Hazard. Mater.* **192**, 538–544 (2011).
38. Huang, H. *et al.* Ce and F comodification on the crystal structure and enhanced photocatalytic activity of Bi₂WO₆ photocatalyst under visible light irradiation. *J. Phys. Chem. C* **118**, 14379–14387 (2014).
39. Li, L. *et al.* Sub-10 nm rutile titanium dioxide nanoparticles for efficient visible-light-driven photocatalytic hydrogen production. *Nat. Commun.* **6**, 5881 (2015).
40. Nguyen, S. D., Yeon, J., Kim, S.-H. & Halasyamani, P. S. BiO(IO₃): a new polar iodate that exhibits an aurivillius-type (Bi₂O₂)²⁺ layer and a large SHG response. *J. Am. Chem. Soc.* **133**, 12422–12425 (2011).
41. Phelan, W. A. *et al.* Stacking variants and superconductivity in the Bi–O–S system. *J. Am. Chem. Soc.* **135**, 5372–5374 (2013).
42. Kim, H. G., Hwang, D. W. & Lee, J. S. An undoped, single-phase oxide photocatalyst working under visible light. *J. Am. Chem. Soc.* **126**, 8912–8913 (2004).
43. Fu, H., Pan, C., Yao, W. & Zhu, Y. Visible-light-induced degradation of Rhodamine B by nanosized Bi₂WO₆. *J. Phys. Chem. B* **109**, 22432–22439 (2005).
44. Yi, Z. *et al.* An orthophosphate semiconductor with photooxidation properties under visible-light irradiation. *Nat. Mater.* **9**, 559–564 (2010).
45. Sheng, J., Li, X. & Xu, Y. Generation of H₂O₂ and OH radicals on Bi₂WO₆ for phenol degradation under visible light. *ACS Catal.* **4**, 732–737 (2014).
46. Kudo, A. & Hijii, S. H₂ or O₂ evolution from aqueous solutions on layered oxide photocatalysts consisting of Bi³⁺ with 6s² configuration and d⁰ transition metal ions. *Chem. Lett.* **28**, 1103–1104 (1999).
47. Zhang, N., Ciriminna, R., Pagliaro, M. & Xu, Y.-J. Nanochemistry-derived Bi₂WO₆ nanostructures: towards production of sustainable chemicals and fuels induced by visible light. *Chem. Soc. Rev.* **43**, 5276–5287 (2014).
48. Kresse, G. & Furthmüller, J. Efficient iterative schemes for *ab initio* total-energy calculations using a plane-wave basis set. *Phys. Rev. B* **54**, 11169–11186 (1996).
49. Kresse, G. & Hafner, J. *Ab initio* molecular dynamics for liquid metals. *Phys. Rev. B* **47**, 558–561 (1993).

Acknowledgements

This work was financially supported by the National Natural Science Foundation of China (Grant numbers U1305242, 21173044 and 21073035).

Author contributions

X.X.W. and Y.G.Z. designed the project; Y.G.Z. conducted the most experiments; Y.F.Z. carried out the theoretical calculations; M.S.L. performed part of the experiments; J.L.L., Z.Z.Z., and H.X.L. supported the experiments and helped to analyse the results; Y.G.Z., X.X.W. together wrote and revised the manuscript with input from all the authors. J.C.S.W. took part in the revision of the manuscript.

Additional information

Supplementary Information accompanies this paper at <http://www.nature.com/naturecommunications>

Competing financial interests: The authors declare no competing financial interests.

Reprints and permission information is available online at <http://npg.nature.com/reprintsandpermissions/>

How to cite this article: Zhou, Y. *et al.* Monolayered Bi₂WO₆ nanosheets mimicking heterojunction interface with open surfaces for photocatalysis. *Nat. Commun.* **6**:8340 doi: 10.1038/ncomms9340 (2015).



This work is licensed under a Creative Commons Attribution 4.0 International License. The images or other third party material in this article are included in the article's Creative Commons license, unless indicated otherwise in the credit line; if the material is not included under the Creative Commons license, users will need to obtain permission from the license holder to reproduce the material. To view a copy of this license, visit <http://creativecommons.org/licenses/by/4.0/>